The Evolution of Rotation and Magnetic Activity in 94 Aqr Aa from Asteroseismology with TESS

Travis S. Metcalfe,[1,2,3] Jennifer L. van Saders,[4] Sarbani Basu,[5] Derek Buzasi,[6] William J. Chaplin,[7,8] Ricky Egeland,[9] Rafael A. Garcia,[10,11] Patrick Gaulme,[3] Daniel Huber,[4] Timo Reinhold,[3] Hannah Schunker,[3,12] Keivan G. Stassun,[13] Thierry Appourchaux,[14] Warrick H. Ball,[7,8] Timothy R. Bedding,[15,8] Sébastien Deheuvels,[16] Lucía González-Cuesta,[17,18] Rasmus Handberg,[8] Antonio Jiménez,[17,18] Hans Kjeldsen,[8,19] Tanda Li,[15,8,20] Mikkel N. Lund,[8] Savita Mathur,[17,18] Benoit Mosser,[21] Martin B. Nielsen,[7,8,22] Anthony Noll,[16] Zeynep Çelik Orhan,[23] Sibel Örtel,[23] Ângela R. G. Santos,[1] Mutlu Yildiz,[23] Sallie Baliunas,[24] and Willie Soon[24]

[1] Space Science Institute, 4765 Walnut St., Suite B, Boulder, CO 80301, USA

[2] White Dwarf Research Corporation, 3265 Foundry Pl., Unit 101, Boulder, CO 80301, USA

[3] Max-Planck-Institut für Sonnensystemforschung, Justus-von-Liebig-Weg 3, 37077, Göttingen, Germany

[4] Institute for Astronomy, University of Hawai'i, 2680 Woodlawn Drive, Honolulu, HI 96822, USA

[5] Department of Astronomy, Yale University, PO Box 208101, New Haven, CT 06520-8101, USA

[6] Department of Chemistry and Physics, Florida Gulf Coast University, 10501 FGCU Blvd S, Fort Myers, FL 33965

[7] School of Physics & Astronomy, University of Birmingham, Edgbaston, Birmingham B15 2TT, UK

[8] Stellar Astrophysics Centre, Aarhus University, Ny Munkegade 120, DK-8000 Aarhus C, Denmark

[9] High Altitude Observatory, National Center for Atmospheric Research, P.O. Box 3000, Boulder, CO 80307-3000, USA

[10] IRFU, CEA, Université Paris-Saclay, F-91191 Gif-sur-Yvette, France

[11] AIM, CEA, CNRS, Université Paris-Saclay, Université Paris Diderot, Sorbonne Paris Cité, F-91191 Gif-sur-Yvette, France

[12] School of Mathematical and Physical Sciences, University of Newcastle, Callaghan, New South Wales, Australia

[13] Vanderbilt University, Department of Physics & Astronomy, 6301 Stevenson Center Lane, Nashville, TN 37235, USA

[14] Institut d'Astrophysique Spatiale, UMR8617, Bâtiment 121, 91045 Orsay Cedex, France

[15] Sydney Institute for Astronomy, School of Physics, University of Sydney 2006, Australia

[16] IRAP, Université de Toulouse, CNRS, CNES, UPS, Toulouse, France

[17] Instituto de Astrofísica de Canarias, La Laguna, Tenerife, Spain

[18] Dpto. de Astrofísica, Universidad de La Laguna, La Laguna, Tenerife, Spain

[19] Institute of Theoretical Physics and Astronomy, Vilnius University, Sauletekio av. 3, 10257 Vilnius, Lithuania

[20] Key Laboratory of Solar Activity, National Astronomical Observatories, Chinese Academy of Science, Beijing 100012, China

[21] LESIA, Observatoire de Paris, Université PSL, CNRS, Sorbonne Université, Université de Paris, 92195 Meudon, France

[22] Center for Space Science, NYUAD Institute, New York University Abu Dhabi, PO Box 129188, Abu Dhabi, United Arab Emirates

[23] Department of Astronomy and Space Sciences, Science Faculty, Ege University, 35100 Bornova, İzmir, Turkey

[24] Harvard-Smithsonian Center for Astrophysics, Cambridge, MA 02138, USA

ABSTRACT

Most previous efforts to calibrate how rotation and magnetic activity depend on stellar age and mass have relied on observations of clusters, where isochrones from stellar evolution models are used to determine the properties of the ensemble. Asteroseismology employs similar models to measure the properties of an individual star by matching its normal modes of oscillation, yielding the stellar age and mass with high precision. We use 27 days of photometry from the *Transiting Exoplanet Survey Satellite* (TESS) to characterize solar-like oscillations in the G8 subgiant of the 94 Aqr triple system. The resulting stellar properties, when combined with a reanalysis of 35 years of activity measurements from the Mount Wilson HK project, allow us to probe the evolution of rotation and magnetic activity in the system. The asteroseismic age of the subgiant agrees with a stellar isochrone fit, but the rotation period is much shorter than expected from standard models of angular momentum evolution. We conclude that weakened magnetic braking may be needed to reproduce the stellar properties, and that evolved subgiants in the hydrogen shell-burning phase can reinvigorate large-scale dynamo action and briefly sustain magnetic activity cycles before ascending the red giant branch.

1. INTRODUCTION

Studies of long-term magnetic variability in solar-type stars rely on measurements of chromospheric activity obtained over many decades. Fortunately, the collection of such observations started in the late 1960s from the Mount Wilson Observatory (Wilson 1978) and continued for more than 35 years. A similar program at Lowell Observatory (Hall et al. 2007) began in the early 1990s and is still ongoing, with the composite time-series for some stars now approaching half a century (Egeland 2017). With sufficiently frequent sampling during each observing season, the modulation from individual active regions can reveal the stellar rotation period (Baliunas et al. 1983), while changes between seasons can constrain latitudinal differential rotation from the slow migration of active regions through the magnetic cycle (Donahue et al. 1996). Such long-term data sets have provided high-quality snapshots of magnetic variability in dozens of solar-type stars (Böhm-Vitense 2007; Brandenburg et al. 2017), but the evolutionary thread that connects them is difficult to establish due to uncertainties in the basic stellar properties such as mass and age (Metcalfe & van Saders 2017).

Asteroseismology with the *Transiting Exoplanet Survey Satellite* (TESS, Ricker et al. 2014) is poised to revolutionize our understanding of the evolution of magnetic variability in solar-type stars. It provides nearly uninterrupted time-series photometry with a 2-minute cadence spanning at least 27 days, which is sufficient to detect solar-like oscillations in many F- and G-type dwarfs and subgiants down to V∼7 (Schofield et al. 2019). The detection of global oscillation properties such as the frequency of maximum oscillation power (ν_{max}) and the mean frequency spacing between consecutive radial overtones ($\Delta\nu$), when combined with spectroscopic properties such as the effective temperature and metallicity (T_{eff}, [Fe/H]), can typically determine the stellar mass with an uncertainty of 6% and the stellar age within about 20% (Serenelli et al. 2017). The identification of individual oscillation frequencies can cut these uncertainties in half (Creevey et al. 2017), and even larger improvements in the age precision are possible for subgiants that exhibit mixed-modes, which couple gravity-driven g mode oscillations in the stellar core with pressure-driven p mode oscillations in the envelope (Deheuvels & Michel 2011; Li et al. 2019).

In this paper, we demonstrate the power of combining ground-based magnetic variability data with asteroseismic measurements of basic stellar properties from TESS. Our initial application is to the 94 Aqr triple system (HD 219834), which includes a blended primary consisting of a G8 subgiant (Aa) and a K3 dwarf (Ab)

in a 6.3 year orbit, and a resolved secondary K2 dwarf (B) separated by 13 arcseconds (Fuhrmann 2008). In Section 2 we provide an overview of the observations, and in Section 3 we reanalyze the archive of chromospheric activity measurements from the Mount Wilson survey (Baliunas et al. 1995) for both the blended primary (A) and the resolved secondary (B) to determine the activity cycle and rotation periods. All three components are blended in the TESS observations, but the subgiant produces the only detectable asteroseismic signal because the K dwarfs oscillate with a much lower amplitude and higher frequency. In Section 4 we analyze and model the subgiant oscillations to determine the basic stellar properties from asteroseismology, and in Section 5 we establish the accuracy of these results with independent estimates of the subgiant radius, mass and age. In Section 6 we combine the rotation period from Mount Wilson data with the stellar mass and age from TESS to model the angular momentum evolution of the subgiant, demonstrating that weakened magnetic braking (van Saders et al. 2016) may be needed to explain the current rotation period. Finally, in Section 7 we summarize and discuss our results, including the idea that evolved subgiants can sustain a "born-again" dynamo before ascending the red giant branch.

2. OBSERVATIONS

2.1. *Mount Wilson HK data*

We use observations from the Mount Wilson Observatory (MWO) HK project (Wilson 1978; Vaughan et al. 1978; Baliunas et al. 1995) to study the long- and short-term variability of magnetic activity in 94 Aqr A and B. The HK Project HKP-1 (1966–1978) and HKP-2 (1978–2003) spectrophotometers obtained counts through 1 Å triangular bandpasses centered on the Ca II H & K (hereafter HK) line cores at 3968.470 Å and 3933.664 Å, respectively, as well as two 20 Å pseudo-continuum bands, R centered at 4001.067 Å, and V centered at 3901.068 Å (Vaughan et al. 1978). Emission in the HK line cores has long been known to be a signature of surface magnetic flux (see Linsky & Avrett 1970, for a review), and the disk-integrated HK emission from the Sun reveals the solar cycle (e.g. White & Livingston 1981; Egeland et al. 2017). The ratio of core to pseudo-continuum counts, $S = \alpha_{\mathrm{MWO}}(N_H + N_K)/(N_R + N_V)$, where α_{MWO} is a calibration factor, defines the now-standard S-index of magnetic activity. The pair 94 Aqr Aa and Ab were not resolved in the MWO observations, so the 94 Aqr A time series represents the sum of surface fluxes from these components. However, the G8 subgiant contributes approximately 97% of the flux in the relevant bandpasses (see Section 5.1).
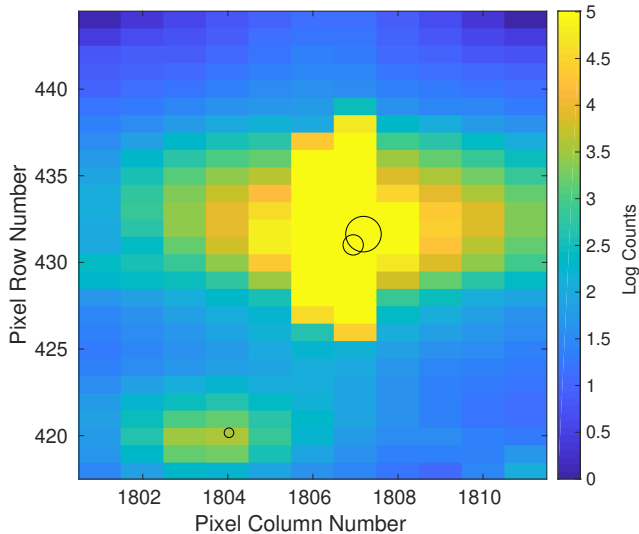
Figure 1. The mean TESS postage stamp ($3'.9 \times 9'.1$) for 94 Aqr, averaged over the complete time series. Counts are shown on a logarithmic scale to allow visibility of the full range, and overlying circles indicate stellar locations from *Gaia* DR2, with a limiting G magnitude of 14. Blending of the A and B components near image center is apparent.

2.2. *TESS photometry*

TESS observed 94 Aqr in 2-minute cadence for 27 days during Sector 2 of Cycle 1 (2018 Aug 22–2018 Sep 20). We used the target pixel files produced by the TESS Science Processing Operations Center (Jenkins et al. 2016) to extract light curves. A preliminary detection of solar-like oscillations was made with a light curve produced using simple aperture photometry, selecting all pixels with flux above three times the median absolute deviation of a median stacked image over the full observing sector. The final light curve was produced using the photometry pipeline[1] (Handberg et al., in prep.) maintained by the TESS Asteroseismic Science Operations Center (TASOC, Lund et al. 2017), which is based on software originally developed to generate light curves from data collected by the *K2* mission (Lund et al. 2015).

Figure 1 shows the postage stamp for 94 Aqr. The large TESS pixels mean that the components of the 94 Aqr system are separated by less than one pixel on the detector. However, we made an effort to extract separate light curves for the two components. We built custom aperture masks around well-separated portions of the combined stellar image, conducted photometric extractions using those masks, and detrended the resulting light curves against spacecraft pointing data using a second-order two-dimensional polynomial fit, which has

worked well for *Kepler* data in the past (Buzasi et al. 2015). Our goal was to construct aperture masks which were dominated by the wings of the images of the two stars, which might then allow us to separate the two stellar contributions. Despite our detrending efforts, light curves resulting from such aperture masks tended to be dominated by photometric jitter resulting from spacecraft motion, and we were unable to unequivocally separate the target light curves using this approach.

2.3. *Derived luminosity*

We derived an updated luminosity for 94 Aqr Aa from speckle observations of the close ($0''.15$) binary A component and the *Gaia* DR2 parallax of the resolved B component (see Section 5.2). The total V magnitude of the A component is 5.18 ± 0.01 (Fabricius et al. 2002), while the magnitude difference between Aa and Ab from speckle imaging is 3.1 (Tokovinin et al. 2015). The bolometric correction (-0.04) was deduced from an extrapolation of VandenBerg & Clem (2003, their Fig. 26), adopting $T_{\rm eff} = 5461 \pm 40$ K from Gray et al. (2006)[2], the parallax of 94 Aqr B adjusted for a small systematic offset (e.g., Stassun & Torres 2018; Zinn 2019), and interstellar extinction $A_V = 0.02^{+0.07}_{-0.02}$ (see Section 5.1). The luminosity deduced from these parameters is $L_{\rm Aa} = 3.31^{+0.22}_{-0.07} \, L_\odot$.

3. ACTIVITY CYCLES AND ROTATION

The resolved components of the 94 Aqr system (A and B) were observed by the Mount Wilson program during the years 1967–2003. The S-index was measured during annual observing seasons, each covering time spans between two and six months. From these data sets, we used several methods to estimate the activity cycle period and the rotation period for each star.

Each S-index time series shows long-term variability due to magnetic activity cycles. We computed the Lomb-Scargle periodogram of the full S-index time series for each component to search for the activity cycle period. We fit a sinusoid to the data using the highest periodogram peak as the initial period guess. The peak heights at the derived periods were used to estimate the period uncertainties. Following Montgomery & O'Donoghue (1999), we estimated the uncertainty of the peak with frequency f as $\sigma(f) = \sqrt{6/N} \cdot \sigma(m)/(\pi T a)$, where N is the number of data points, T is the time baseline of the observations, and a is the amplitude of

---

[1] https://tasoc.dk/code/

[2] Note that the quoted uncertainty on $T_{\rm eff}$ does not account for systematics between different methods and the fundamental $T_{\rm eff}$ scale set by the accuracy of interferometric angular diameters, which can be $\gtrsim 2\%$ (Casagrande et al. 2014; White et al. 2018).
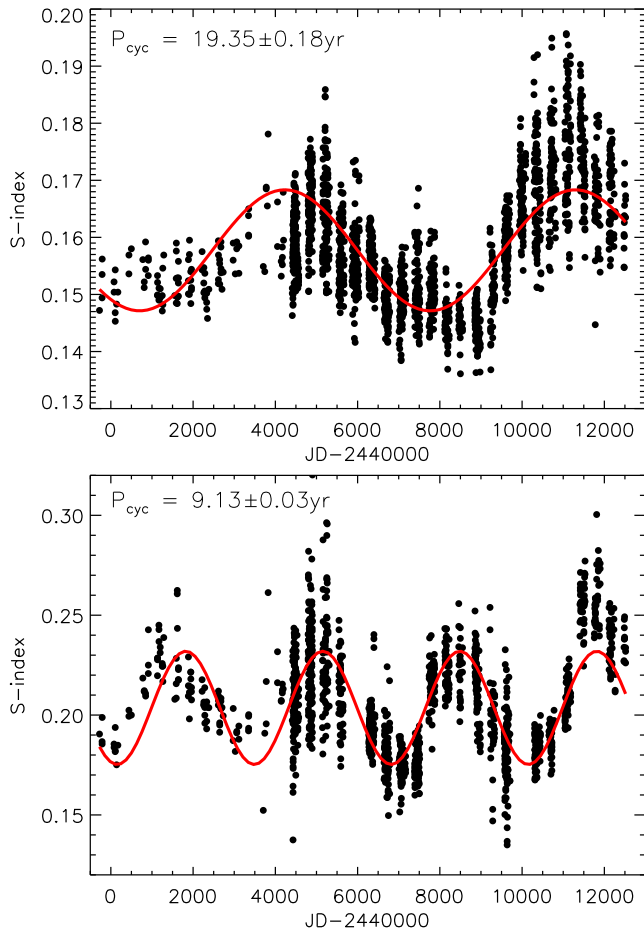
Figure 2. Long-term variability of 94 Aqr A (top) and 94 Aqr B (bottom) from the Mount Wilson S-index data. The reported activity cycle period and uncertainty come from fitting a sinusoid (red curves) to each time series.

the sinusoid. We computed the root-mean-square deviation $\sigma(m) = \sqrt{\sigma^2 \cdot (1 - h_{\rm peak})}$, where σ^2 is the variance of the zero-mean time series, and $h_{\rm peak}$ is the normalized peak height at the derived period. We obtained activity cycle periods of 19.35 ± 0.18 yr and 9.13 ± 0.03 yr for 94 Aqr A and B, respectively (see Figure 2). We validated this analysis with two other methods, the autocorrelation function and a time-period analysis using a Morlet wavelet (Mathur et al. 2010; García et al. 2014; Buzasi et al. 2016). These analyses gave similar results.

The number of data points per observing season at Mount Wilson increased around 1980, revealing large variability which we attribute to active regions rotating in and out of view. From the seasonal data, Baliunas et al. (1996) measured rotation periods of 42 days and 43 days for the A and B components, while Olspert et al. (2018) found 43.4 ± 1.9 days and 34.8 ± 0.9 days, respectively. We performed an independent analysis of the Mount Wilson data sets, with three teams analyzing
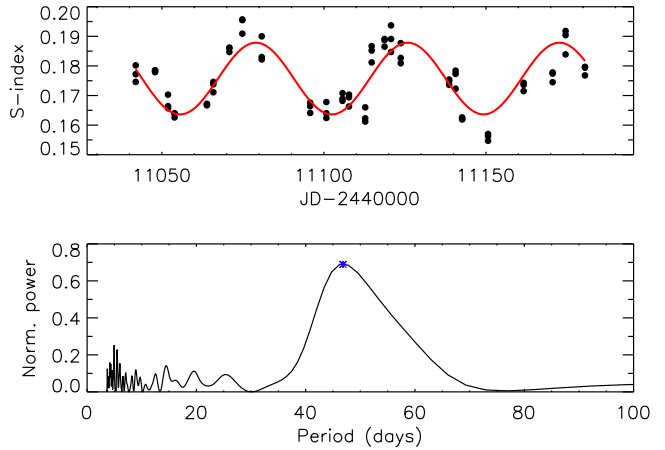
Figure 3. Time series Ca HK measurements of 94 Aqr A from a representative observing season near cycle maximum in 1998 (top). The corresponding periodogram (bottom) shows a clear detection of rotation (blue point) with a period similar to the median value reported in the text. The detected period is shown with a red line in the top panel.

them seasonally and four teams analyzing the complete time series globally. The teams applied a range of different analysis techniques to both stars in the system, including application of the discrete Fourier transform (DFT), performing sinusoid fits to individual seasons and studying a histogram of the results, applying autocorrelation functions, and time-period wavelet analysis. In the case of 94 Aqr A, there was excellent agreement amongst the different methods, and we report a median rotation period of $P_{\rm rot} = 46.9 \pm 1.9$ days (see Figure 3). For 94 Aqr B, the teams could not reach a consensus on the statistical significance of any potential detections of rotation from the seasonal data sets.

For the resolved B component, the activity cycle period can be attributed unambiguously to the K2 dwarf. For the blended A component, the G8 subgiant (Aa) contributes approximately 97% of the flux in the relevant bandpasses (see Section 5.1). Consequently, the 3% of the flux contributed by the K3 dwarf (Ab) would need to vary by roughly an order of magnitude to explain the observed S-index variation of up to 30% on both rotational and activity cycle timescales. Such modulations would be unprecedented (e.g., see Soon et al. 1994), so we identify the G8 subgiant as the source of the S-index variability. Note that comparable rotation periods have been observed in other G-type subgiants, including HD 182572 (41 days, Baliunas et al. 1996), and KIC 8524425 (42 ± 3 days, García et al. 2014). The implications of the observed activity cycle, and the possibility of a "born-again" dynamo in evolved subgiants, are discussed in Section 7.

4. ASTEROSEISMOLOGY OF 94 Aqr Aa

4.1. *Extracting the oscillation parameters*

We compute the power spectral density (PSD) of the TESS light curve (see Section 2.2) to analyze the stellar oscillations. Because the signal to noise ratio (S/N) of the oscillations is relatively low, six teams analyzed the oscillation spectrum to agree on a frequency set. The frequency analysis involves taking into account the background noise caused by surface granulation (e.g., Harvey et al. 1988), then extracting the star's eigenmodes (see Figure 4). Because we are dealing with a subgiant star, the latter involves considering mixed dipolar ($l = 1$) modes, where acoustic waves excited in the convective envelope couple with internal gravity waves in the core.

By definition, a mixed mode has a dual character, being both a p mode and a g mode. The solution of the continuity equation by Shibahashi (1979) led to an implicit expression for the mixed mode frequency ν_{pg} as

$$\tan\theta_p = q\tan\theta_g, \tag{1}$$

where θ_p and θ_g are the phase functions of ν_{pg} with respect to the p mode and g mode frequencies, and q is the coupling factor. The phase function θ_p is given by:

$$\theta_p = \pi\frac{(\nu_{pg} - \nu_{n_{p,1}})}{\Delta\nu(n_p)} \tag{2}$$

where

$$\Delta\nu(n_p) = [1 + \alpha(n_p - n_{\max})]\,\Delta\nu \tag{3}$$

and θ_g is given by:

$$\theta_g = \pi\frac{1}{P_1}\left(\frac{1}{\nu_{pg}} - \frac{1}{\nu_{n_{g,1}}}\right). \tag{4}$$

When there is no coupling, $q = 0$ and there are no mixed modes, so $\nu_{pg} = \nu_{n_{p,1}}$. Otherwise, the solutions to Eq. (1) provide the frequencies of the mixed modes.

Our computation of mixed modes is based upon Mosser et al. (2015). We first assume that the frequencies of radial modes $\nu_{n_p,0}$ are given by:

$$\nu_{n_p,0} = \left[n_p + \epsilon + \frac{\alpha}{2}(n_p - n_{\max})^2\right]\Delta\nu \tag{5}$$

where n_p is the radial order, ϵ is a phase offset, α is the mean curvature of the $l = 0$ pattern as a function of frequency, $n_{\max}$ is the closest radial order to $\nu_{\max}$, and $\Delta\nu$ is the mean large frequency separation between consecutive radial overtones. The frequencies of the dipolar p modes are given by:

$$\nu_{n_p,1} = \nu_{n_p,0} + \left(\frac{1}{2} - d_{01}\right)\Delta\nu \tag{6}$$
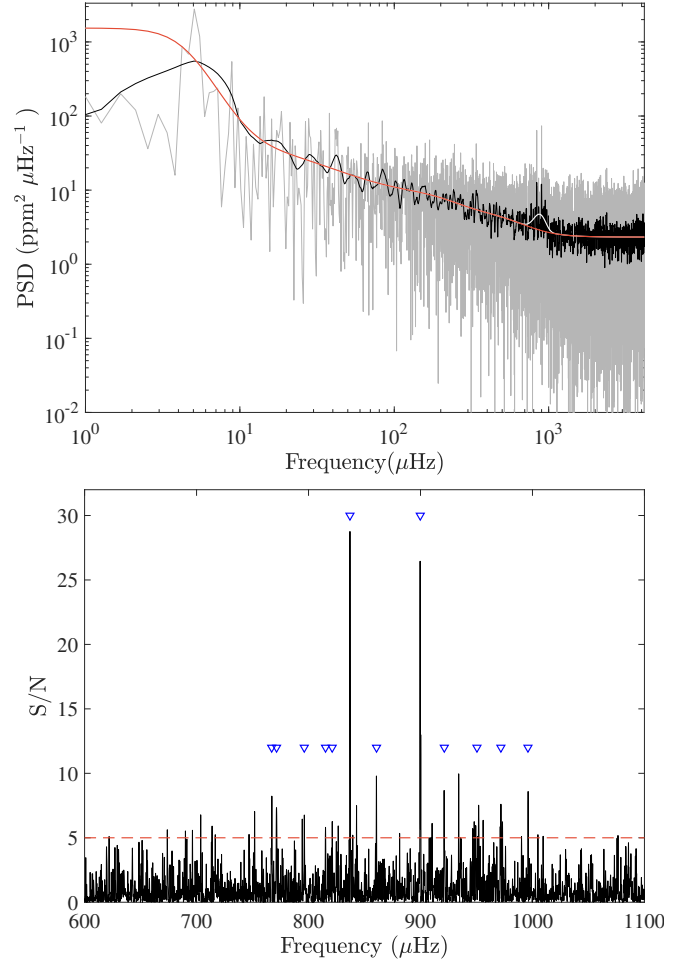

Figure 4. Top: power spectral density (PSD) of the TESS light curve as a function of frequency in μHz. The red line represents a fit to the background noise, and the white line includes the excess power due to oscillations. Bottom: ratio of the power spectrum to the background noise as a function of frequency in the range where oscillation modes are detected. Within this frequency interval, peaks above the red line have $< 1\%$ probability of being due to noise, with the false alarm probability decreasing exponentially at higher S/N.

where d_{01} is the mean separation between $l = 0$ and $l = 1$ modes of a given order n, relative to $\Delta\nu$. The periods of dipolar g modes $P_{n_g,1}$ are given by:

$$P_{n_g,1} = (n_g + \alpha_1)P_1 \tag{7}$$

where n_g is the g mode order, α_1 is a constant and P_1 is the period spacing of dipolar modes. The values deduced from Eq. (1) for 94 Aqr Aa are $P_1 = 290.8\pm0.5$ seconds, with $q = 0.16 \pm 0.025$. These values are similar to stars with comparable $\Delta\nu$ (see Mosser et al. 2014). We used the resulting asymptotic $l = 1$ mode frequencies as a guide for identification and subsequent fitting.

The observed oscillation spectrum is typical of a subgiant star, where all $l = 1$ modes are of mixed nature,

Table 1. Identified Oscillation Frequencies.

n	l	ν_{nl}^{obs} (μHz)	ν_{nl}^{mod} (μHz)	ν_{nl}^{cor} (μHz)
15	0	771.39 ± 0.19	773.63	771.32
16	0	821.62 ± 2.85	826.39	821.73
18	0	921.29 ± 0.23	933.78	921.93
19	0	971.64 ± 0.29	987.71	970.81
15	1	794.37 ± 0.14	801.01	797.96
16	1	837.02 ± 0.12	839.83	837.48
16	1	860.61 ± 0.14	862.92	858.32
17	1	899.76 ± 0.17	909.41	900.14
18	1	950.49 ± 1.21	960.71	947.10
19	1	996.11 ± 0.15	1010.47	994.33
14	2	767.21 ± 0.31	768.71	766.60
15	2	815.28 ± 0.15	821.81	817.46

leading to the impression of an irregular mode distribution as a function of frequency. Due to the rather low S/N, our estimate of the frequency of maximum oscillation power suffers from a relatively large uncertainty at $\nu_{\mathrm{max}} = 875 \pm 12$ μHz. Similarly, the determination of $\Delta\nu$ was initially ambiguous, with estimates ranging from about 40 to 60 μHz. We converged to the value $\Delta\nu = 50.2 \pm 0.4$ μHz, which is simultaneously compatible with a fit to both the radial and non-radial modes.

From a consensus of the individual teams, we identified four radial (l=0), five dipole (l=1), and two quadrupole (l=2) modes above our significance threshold (S/N $\geq$ 5). The identified frequencies from the team that was most representative of the consensus are listed in Table 1 and marked with blue triangles in the bottom panel of Figure 4. The two sets of closely-spaced triangles at the lower end of the frequency range are pairs of l=2 and l=0 modes, while the two largest peaks are strongly mixed l=1 modes. Slightly below the frequency range with identified modes, there are a few marginal peaks that may be additional l=1 and l=2 modes for which we did not reach a consensus. Finally, there are three peaks above our significance threshold that remain unidentified: a relatively strong peak near 935 μHz, a weaker peak adjacent to a mixed mode near 843 μHz, and a marginal peak close to an l=2/l=0 pair at 826 μHz. Future TESS observations in Sector 29 may help to clarify these ambiguities.

4.2. Modeling the oscillation modes

To determine the fundamental properties of 94 Aqr Aa, several teams attempted to match the observed oscillation frequencies identified above, us-

ing stellar evolution models from MESA (Paxton et al. 2011), ASTEC (Christensen-Dalsgaard 2008), and the Yale Rotating Evolution Code (YREC, Demarque et al. 2008) in its non-rotating configuration. We found reasonable agreement between the resulting determinations of asteroseismic radius, mass, and age, with relative dispersions of 2%, 7%, and 22%, respectively. For consistency with our subsequent analysis of the angular momentum evolution (see Section 6), below we provide details only for the results obtained with YREC.

We initially constructed a grid of models with masses in the range 1.16 $M_\odot$ to 1.32 $M_\odot$ with a spacing of 0.01 $M_\odot$. For each mass, models were created with five values of the mixing length parameter spanning $\alpha_{\mathrm{MLT}} =$ 1.5 to 2.3, initial helium abundances from the primordial helium abundance of 0.248 (Steigman 2010) to 0.30 in steps of 0.01, and initial [Fe/H] in the range +0.15 to +0.33 in steps of 0.01. We use the Grevesse & Sauval (1998) solar mixture to convert [Fe/H] to Z/X. For each of the parameters, the models were evolved from the zero-age main-sequence (ZAMS) to an age of 11 Gyr. Models were output at intermediate ages.

The models were constructed using OPAL opacities (Iglesias & Rogers 1996) supplemented with low temperature opacities from Ferguson et al. (2005). The OPAL equation of state (Rogers & Nayfonov 2002) was used. All nuclear reaction rates are obtained from Adelberger et al. (1998), except for that of the $^{14}N(p,\gamma)^{15}O$ reaction, which we adopt from Formicola et al. (2004). All models included gravitational settling of helium and heavy elements using the formulation of Thoul et al. (1994). The oscillation frequencies of the models were calculated with the code of Antia & Basu (1994).

The fits to the observations were done in two steps: we first looked for models that provided a good match to the frequencies of the l=0 and l=2 modes, in addition to showing consistency with spectroscopic constraints (Gray et al. 2006, $T_{\mathrm{eff}} = 5461 \pm 40$ K; [Fe/H] = $+0.23 \pm 0.08$) and the derived luminosity from Section 2.3 ($L_{\mathrm{Aa}} = 3.31^{+0.22}_{-0.07}$ $L_\odot$).

The quality of the fit was defined as follows. For each observable, T_{eff}, [Fe/H] and luminosity L, we define a likelihood. For instance, the likelihood for effective temperature was defined as

$$\mathcal{L}(T_{\mathrm{eff}}) = D \exp(-\chi^2(T_{\mathrm{eff}})/2), \qquad (8)$$

with

$$\chi^2(T_{\mathrm{eff}}) = \frac{(T_{\mathrm{eff}}^{\mathrm{obs}} - T_{\mathrm{eff}}^{\mathrm{mod}})^2}{\sigma_T^2}, \qquad (9)$$

where σ_T is the uncertainty on the effective temperature, and D is a normalization constant. We define the likelihoods for [Fe/H] and L in a similar manner.

Table 2. Stellar Properties of 94 Aqr Aa.

	Asteroseismic	Other	Source
Radius ($R_\odot$)	2.06 ± 0.03	2.07 ± 0.13	(1)
Mass ($M_\odot$)	1.22 ± 0.03	1.24 ± 0.08	(2)
Age (Gyr)	6.2 ± 0.2	$6.2^{+0.9}_{-0.7}$	(3)
$T_{\rm eff}$ (K)	5411 ± 31	5461 ± 40	(4)
[Fe/H] (dex)	$+0.15 \pm 0.05$	$+0.23 \pm 0.08$	(4)
Luminosity ($L_\odot$)	3.30 ± 0.06	$3.31^{+0.22}_{-0.07}$	(5)
$\alpha_{\rm MLT}$	1.78 ± 0.20	$\cdots$	

References—(1) Section 5.1; (2) Section 5.2; (3) Section 5.3; (4) Gray et al. (2006); (5) Section 2.3

For the frequencies, we first corrected for surface effects using the two-term surface correction proposed by Ball & Gizon (2014)

$$\delta\nu_{nl} \equiv \nu_{nl}^{\rm obs} - \nu_{nl}^{\rm mod} \qquad (10)$$

$$= \frac{1}{I_{nl}} \left[a \left(\frac{\nu_{nl}}{\nu_{\rm ac}} \right)^{-1} + b \left(\frac{\nu_{nl}}{\nu_{\rm ac}} \right)^3 \right], \qquad (11)$$

where $\delta\nu_{nl}$ is the difference in frequency for a mode of degree l and radial order n between the observations and the model, ν_{nl} is the frequency and I_{nl} is the inertia of the mode, and $\nu_{\rm ac}$ is the acoustic cut-off frequency, with coefficients a and b determined from a generalized least-squares fit to the frequency difference of the $l = 0$ modes. This allows us to define a likelihood for frequencies. We define $\nu_{nl}^{\rm cor} = \nu_{nl}^{\rm mod} - S$, where S is defined by the right-hand side of Eq. (11) but now applied to both $l = 0$ and $l = 2$ modes.

$$\chi^2(\nu) = \frac{(\nu_{nl}^{\rm obs} - \nu_{nl}^{\rm cor})^2}{\sigma_{nl}^{\rm obs}}. \qquad (12)$$

Consequently

$$\mathcal{L}(\nu) = C \exp\left(-\frac{\chi^2(\nu)}{2} \right), \qquad (13)$$

where C is a normalization constant.

The total likelihood for each model is then

$$\mathcal{L}_{\rm total} = \mathcal{L}(\nu)\mathcal{L}(T_{\rm eff})\mathcal{L}([{\rm Fe/H}])\mathcal{L}(L). \qquad (14)$$

The medians of the marginalized likelihoods of the ensemble of models were used to determine the most likely stellar properties, after converting them to a probability density by normalizing the likelihood by the prior distribution of each parameter.

A finer grid in mass and age was created around the most likely values of these parameters in order to fit
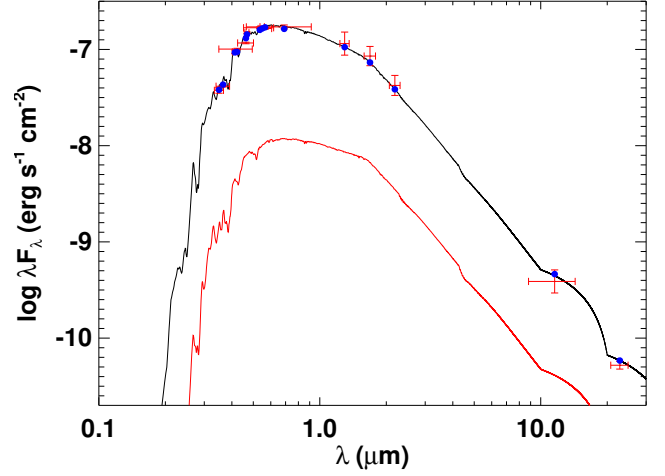
Figure 5. Spectral energy distribution (SED) fit to the broadband photometry of 94 Aqr A. The fit to 94 Aqr Aa is shown in black, with observed fluxes as red symbols and bandpass integrated model fluxes as blue symbols. The red curve shows the SED of the companion (Ab), which is used to correct for light contamination in the SED of 94 Aqr Aa.

the $l = 1$ modes, improving both the accuracy of the stellar age and the sampling of the posterior distributions. The likelihoods were calculated again, except that now in Eq. (12) we also used the $l = 1$ modes. The optimal asteroseismic properties were derived from the new probability density, and they are listed in Table 2 along with independent estimates (see Section 5) and the other available constraints. Note that because YREC did not use a global optimization technique, it is possible that a better fit to the observations exists.

5. ACCURACY OF THE STELLAR PROPERTIES

5.1. *Radius from SED*

We performed a fit to the broadband photometry of 94 Aqr A in order to make an independent determination of the stellar radius (see Figure 5). We followed the procedures described in Stassun & Torres (2016); Stassun et al. (2017, 2018). Briefly, we adopted the best available spectroscopic values for $T_{\rm eff}$ and [Fe/H], and then fit a standard stellar atmosphere model (Kurucz 1992) to the broadband spectral energy distribution (SED) in order to determine empirically the bolometric flux at Earth ($F_{\rm bol}$). The free parameter of the fit was the interstellar extinction. Using the *Gaia* DR2 parallax, adjusted for the known small systematic offset ($-82\ \mu$as, Stassun & Torres 2018), the stellar radius was then determined via the Stefan-Boltzmann relation.

We adopted the Johnson UBV magnitudes from the Mermilliod (2006) homogenized photometric catalog of bright stars, the $B_T V_T$ magnitudes from Tycho-2, the

Table 3. Orbital Parameters of 94 Aqr A.

Parameter	Value
Period (years)	6.298 ± 0.005
T (year)	2012.310 ± 0.05
e	0.1621 ± 0.0056
a (arcsec)	0.1928 ± 0.0036
i (°)	47.26 ± 1.92
Ω (°)	343.95 ± 1.10
ω (°)	31.50 ± 2.64
K (km s^{-1})	6.030 ± 0.038
π (mas)	44.515 ± 0.055

Figure 6. Results of a simultaneous fit to the astrometry (top) and spectroscopy (bottom) of 94 Aqr A. Data are shown with blue points, and the fit is shown in black.

Strömgren *ubvy* magnitudes from Paunzen (2015), the JHK_S magnitudes from 2MASS, the W3–W4 magnitudes from WISE, and the G magnitude from *Gaia*. Together, the available photometry spans the full stellar SED over the wavelength range 0.35–22 μm.

We adopted the spectroscopic parameters from Gray et al. (2006), doubling the quoted uncertainty on $T_{\rm eff}$ to a more realistic 80 K. We also adopted the parameters for the blended Ab component from Docobo et al. (2018), and similarly fit its SED, in order to correct the $F_{\rm bol}$ of 94 Aqr Aa for contamination of light in the broadband photometry from the close companion.

The fit has a reduced $\chi^2 = 3.3$ and an extinction of $A_V = 0.02^{+0.07}_{-0.02}$. The resulting bolometric flux is $F_{\rm bol} = (2.18 \pm 0.25) \times 10^{-7}$ erg s^{-1} cm^{-2}, which with the parallax gives $R_{\rm Aa} = 2.07 \pm 0.13\ R_\odot$, consistent with the asteroseismic value ($R = 2.06 \pm 0.03\ R_\odot$). A similar analysis of 94 Aqr B, adopting the spectroscopic constraints from Fuhrmann (2008), yields $R_{\rm B} = 0.85 \pm 0.03\ R_\odot$.

5.2. *Mass from astrometry and spectroscopy*

To derive the individual masses of 94 Aqr Aa and Ab, we used the available data from astrometry and spectroscopy. For astrometry, we used the same data available to Docobo et al. (2018). For spectroscopy, we used radial velocities measured by Sarma (1962) and Katoh et al. (2013). We then jointly fit the astrometric and spectroscopic data using an MCMC approach as described in Marcadon et al. (2018). The orbital parameters are given in Table 3, and the results are illustrated in Figure 6.

Docobo et al. (2018) used the *Gaia* parallax for the Aa/Ab system to derive the masses of the two components. Unfortunately, *Gaia* DR2 does not account for binarity. This means the parallax of 94 Aqr A is not useful, because the period of the orbit is about 6.3 years. Instead, we used the parallax of 94 Aqr B
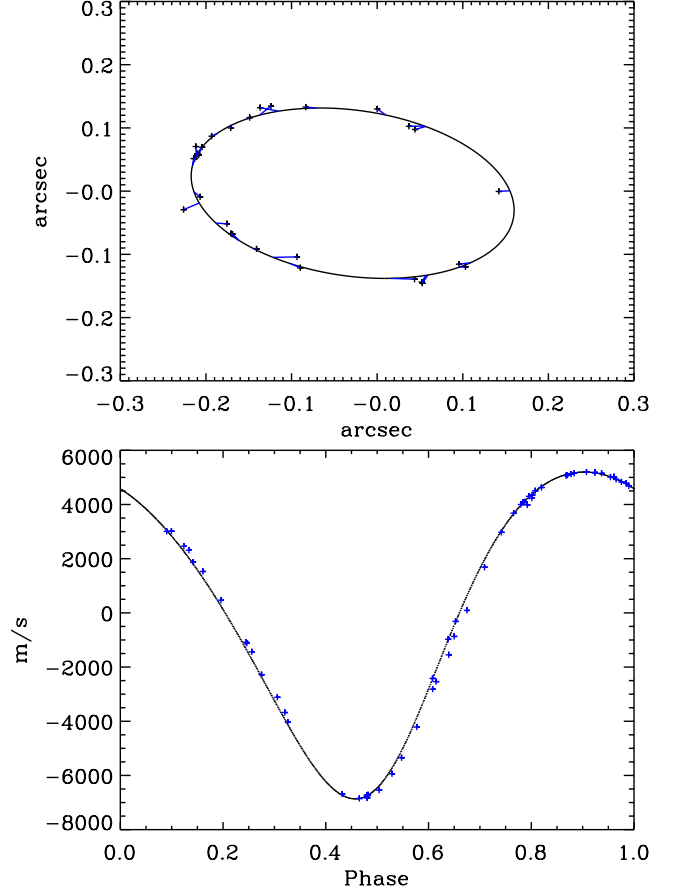
($\pi = 44.515 \pm 0.055$ mas; Gaia Collaboration et al. 2018), which has an orbital period around A that is longer than a few hundred years (Mason et al. 2001).

We derived individual masses for Aa and Ab following the same approach as Docobo et al. (2018). The error propagation was done using the MCMC solution, thereby taking into account the intrinsic correlations between the various orbital parameters. We found $M_{\rm Aa} = 1.24 \pm 0.08\ M_\odot$, in agreement with the asteroseismic value ($M = 1.22 \pm 0.03\ M_\odot$), and $M_{\rm Ab} = 0.81 \pm 0.04\ M_\odot$.

5.3. *Age from isochrone fitting*

Because 94 Aqr Aa is on the subgiant branch and experiencing relatively rapid evolution, its age is well constrained from simple isochrone fitting. We use the methods described in Section 6 to find a best fit stellar model from the observed surface constraints on radius, $T_{\rm eff}$, and [Fe/H] in the "Other" column of Table 2. We adopt a broad prior on the age of 5.0 ± 5.0 Gyr, while the priors on mass, [Fe/H], and mixing length are taken directly from Table 2. We estimate an age of

$t_{iso} = 6.2^{+0.9}_{-0.7}$ Gyr, which is consistent with the asteroseismic value ($t = 6.2 \pm 0.2$ Gyr).

6. ANGULAR MOMENTUM EVOLUTION

By combining the stellar properties from asteroseismology with the rotation period determined from the Mount Wilson HK data, we can finally model the angular momentum evolution of 94 Aqr Aa using magnetic braking formulations from van Saders & Pinsonneault (2013), van Saders et al. (2016) and van Saders et al. (2019). We examined two distinct classes of braking models: "standard" and "weakened" magnetic braking.

The standard models are described in van Saders & Pinsonneault (2013). We model rotational evolution using the `rotevol` code (as in van Saders & Pinsonneault 2013; van Saders et al. 2016; Somers & Pinsonneault 2016) atop formally non-rotating YREC stellar evolution tracks manipulated with the isochrone tools in `kiauhoku` (Claytor et al. 2020). The stellar model grid physics are the same as described in van Saders & Pinsonneault (2013) with the addition of gravitational settling and diffusion, the wider metallicity range of van Saders et al. (2016), and an Eddington atmosphere. The magnetic braking law has four free parameters which are tuned to reproduce the observed rotation periods in young open clusters and the Sun: the overall normalization of the braking law, f_k; the period and duration of the disk locking phase P_{disk} and T_{disk}, which set the initial rotation rate; and the angular rotation velocity at which the spin-down transitions from the saturated to unsaturated regime, ω_{crit}. For stars near or beyond the end of the main-sequence, only f_k is important; the strong dependence of the spin-down on rotational velocity means that the late-time evolution is insensitive to variations in parameters that affect early-time evolution (ω_{crit}, T_{disk}, P_{disk}). In this prescription, the spin-down is smooth at late times in much the same manner as fully empirical gyrochronology relations (e.g., Barnes 2010).

The weakened braking models are identical to the standard models except for one additional free parameter that affects the late-time evolution: a critical Rossby number Ro_{crit} beyond which magnetic braking ceases and angular momentum is conserved. Due to the weakened braking, the modified model generally predicts faster rotation periods than the standard model, which allows it to reproduce the rotation periods of old asteroseismic calibrator stars (van Saders et al. 2016). With a fixed $f_k = 6.6$ (and $\omega_{crit} = 3.4 \times 10^{-5}$ s^{-1}, $P_{disk} = 8.1$, $T_{disk} = 0.28$), van Saders et al. (2016) found $Ro_{crit} = 2.16$ when calibrating against 21 *Kepler* asteroseismic targets.
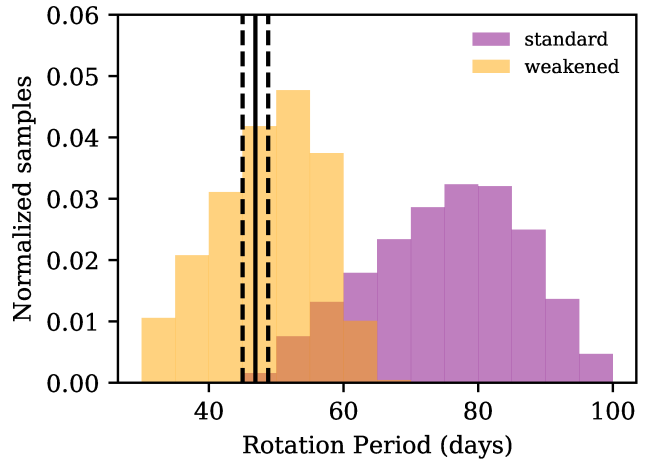
Figure 7. Predictions from a standard spin-down model (purple) and weakened braking model (orange) for the rotation period of 94 Aqr Aa. The observed rotation period from Mount Wilson data is shown with black vertical lines.

6.1. *Rotational modeling of 94 Aqr Aa*

For 94 Aqr Aa, we used the asteroseismically constrained properties to predict the observed rotation period under the two different braking prescriptions. In contrast to the main-sequence, envelope expansion on the subgiant branch (SGB) increasingly dominates over magnetic braking in the rotational evolution as the star approaches the base of the giant branch. This means that the predicted rotation is tied strongly to age, but also to both HR diagram position and stellar mass.

We used a Monte Carlo approach (`emcee`, Foreman-Mackey et al. 2013) to search our model grids in mass, age, bulk composition (Z/X), and mixing length (α_{MLT}) to match the best fit values of T_{eff}, [Fe/H], and radius from the "Asteroseismic" column in Table 2. We adopted Gaussian priors on the mass, age, [Fe/H], and α_{MLT} centered on 1.22 $M_{\odot}$, 6.2 Gyr, +0.15 dex, and 1.78 with 1σ widths of 0.03 $M_{\odot}$, 0.2 Gyr, 0.05 dex, and 0.2, respectively. A total of 8 chains were run for 100000 steps each, with the first 5000 steps discarded as burn-in. Such a run corresponds to > 1000 autocorrelation times in all variables of interest.

We predict a rotation period for the standard braking model of $P = 76^{+11}_{-13}$ days with the asteroseismic surface constraints. For a weakened braking model with Ro_{crit}, we predict $P = 49^{+7}_{-9}$ days, in good agreement with the observed period of 46.9 ± 1.9 days (see Figure 7). If instead we adopt the spectroscopic values for T_{eff} and [Fe/H], we would predict $P = 63^{+12}_{-11}$ days for the standard model, and $P = 41 \pm 8$ days for weakened braking. In both cases the weakened braking model provides better agreement with the observed rotation.

6.2. Robustness to assumptions

There are two types of physical assumptions that can affect our conclusions: assumptions about the magnetic braking and angular momentum transport itself, and physical uncertainties in the underlying stellar models. We argue that the latter are of most concern for the weakened braking interpretation.

We have made a host of assumptions about the braking, most of which we expect cannot shift the standard model prediction toward the shorter observed rotation period. We've assumed a single set of initial conditions despite the fact that stars in nature display a range of birth rotation rates, but even if we had launched our best fit models rotating at breakup velocity on the ZAMS (3 times faster than assumed in our models, which have a ZAMS period of less than 1 day) the predicted period for the standard model would differ by only 1 day. We haven't allowed for differential rotation, but for cases in which the core rotationally decouples from the envelope (e.g. Denissenkov et al. 2010; MacGregor & Brenner 1991) we expect slower observed envelope rotation rates, not faster (Deheuvels et al. 2014). If the star had a strong radial differential rotation on the main-sequence it could result in faster-than-expected rotation on the SGB, but indications are that main-sequence and early SGB stars have little radial differential rotation (e.g. Thompson et al. 1996; Saio et al. 2015; Benomar et al. 2015; Deheuvels et al. 2020). 94 Aqr Aa is not a single star, but its 6.3 year orbit is sufficiently wide that we expect it to behave as a single star in terms of rotational evolution.

By contrast, reasonable changes to the underlying stellar physics have the ability to shift the predicted rotation period in the standard model by more than 10 days. The asteroseismic fits in Section 4.2 allowed the mixing length to be a free parameter, rather than fixing it to the solar value as is the norm in most non-seismic analyses. We have found that our results are sensitive to the choice of mixing length.

Smaller values of α_{MLT} yield models with shorter periods. Changing the mixing length tends to shift subgiant tracks along the SGB, meaning that constraints in temperature, radius, and luminosity can be matched with a model of essentially the same stellar mass. However, at a fixed location in the HR diagram, models of the same mass but different mixing lengths will have different convective overturn timescales, affecting the predicted rotation period. A $1.2\,M_\odot$, 0.2 dex model at $2.0\,R_\odot$ with a mixing length of 1.8 has a period of 60 days, but the same model with a mixing length of 1.6 has a period of 46 days at $2.0\,R_\odot$— a difference comparable to that between period predictions for a standard and weakened

model of magnetic braking. While we have allowed the mixing length to vary in our fit and incorporated the (fairly broad) asteroseismic prior on α_{MLT}, the sensitivity of the period to the choice of mixing length means that we cannot rule out the possibility that the tension between the observed and predicted period for standard braking arises from an inappropriate choice of the mixing length.

Efforts to quantify how the mixing length should vary as a function of stellar properties have yielded conflicting results. Observational estimates from asteroseismology (Bonaca et al. 2012; Creevey et al. 2017; Tayar et al. 2017; Viani et al. 2018) find that the mixing length should increase as the metallicity increases, while simulations of convection generally arrive at the opposite conclusion (Magic et al. 2015). Viani et al. (2018) predicts that a star with the surface gravity, temperature and metallicity of 94 Aqr Aa should have a supersolar mixing length for any of the relations they provide. Larger mixing lengths result in longer rotation periods, and would reinforce the tension between the standard model and the observed rotation. We note that, in contrast to these predictions, the asteroseismic mixing length for 94 Aqr Aa in Table 2 is sub-solar ($\alpha_{\mathrm{MLT},\odot} = 1.98$).

The apparent need for weakened braking could also be spurious if our stellar mass is underestimated. Rotation rate is a very strong function of mass, particularly near the Kraft (1967) break, where stars above the break in mass rotate rapidly, while less massive stars rotate more slowly. The dichotomy is a result of the diminishing convective envelopes in more massive stars, and the consequently weak large-scale fields and magnetic braking. If we fix the mixing length to $\alpha_{\mathrm{MLT}} = 1.78$ and broaden the priors on mass, age, and metallicity to 1σ Gaussian widths of $0.5\,M_\odot$, 2.0 Gyr, and 0.2 dex, the resulting increase of $0.05\,M_\odot$ in mass is sufficient to shift the predicted rotation period from ∼71 days to 55 days. However, we note that changing the mixing length to ∼1.5 can match the observed rotation period with no upward adjustment to the mass, so we consider the poorly constrained mixing length to be the more intractable source of uncertainty.

These issues are connected to challenges inherent in stellar modeling that have stood for decades, and the solution is unlikely to emerge from this article. In the following section, we explore the possibility that 94 Aqr Aa has experienced weakened magnetic braking, but we caution the reader about the sizable caveats to this interpretation that we have outlined above.

7. SUMMARY AND DISCUSSION

By combining Mount Wilson observations of magnetic variability with TESS asteroseismic measurements of the G8 subgiant 94 Aqr Aa, we have discovered new evidence for weakened magnetic braking (van Saders et al. 2016) and the possibility of a "born-again" dynamo in evolved stars, as we discuss below.

A reanalysis of 35 years of HK observations (Section 3) yielded rotation and magnetic activity cycle periods for 94 Aqr Aa ($P_{rot}^{Aa} = 46.9 \pm 1.9$ days, $P_{cyc}^{Aa} = 19.35 \pm 0.18$ yr) and a cycle period for 94 Aqr B ($P_{cyc}^{B} = 9.13 \pm 0.03$ yr). The amplitude of the observed variability in the blended A component allowed us to attribute these properties to the subgiant (Aa) because it contributes 97% of the light in the relevant bandpasses.

Asteroseismology of 94 Aqr Aa from TESS observations (Section 4) yielded precise determinations of the stellar radius ($R = 2.06 \pm 0.03 \, R_\odot$), mass ($M = 1.22 \pm 0.03 \, M_\odot$) and age ($t = 6.2 \pm 0.2$ Gyr). We established the absolute accuracy of these properties (Section 5) with independent estimates of the stellar radius from SED fitting ($R_{Aa} = 2.07 \pm 0.13 \, R_\odot$), the stellar mass from a close binary orbit ($M_{Aa} = 1.24 \pm 0.08 \, M_\odot$), and the age from isochrone fitting ($t_{iso} = 6.2_{-0.7}^{+0.9}$ Gyr).

Using the asteroseismic properties from Section 4, we attempted to reproduce the observed rotation period from Section 3 with angular momentum evolution models (Section 6) that adopted either standard spin-down or the weakened magnetic braking proposed by van Saders et al. (2016). The standard model predicts a rotation period ($P = 76_{-13}^{+11}$ days) that is substantially longer than suggested by the observations, while the model with weakened magnetic braking ($P = 49_{-9}^{+7}$ days) more closely reproduces the observed rotation period with stalled spin-down at a critical Rossby number $Ro_{crit} = 2.16$ (van Saders et al. 2016). Note that with these models, the Rossby number of the Sun is $Ro_\odot \sim 2.2$, comparable to the critical value.

The fact that the G8 subgiant shows a magnetic activity cycle provides an interesting constraint on stellar dynamo models. According to the scenario proposed by Metcalfe & van Saders (2017), activity cycles should gradually grow longer with the rotation period along the two sequences identified by Böhm-Vitense (2007). When a star reaches the critical Rossby number suggested by van Saders et al. (2016), the rotation period remains relatively constant while the activity cycle appears to grow longer and weaker before disappearing entirely. The resulting "flat activity" star still shows magnetic activity on small scales, allowing rotation periods to be measured, but the mean activity level is approximately constant on longer timescales. Such stars have
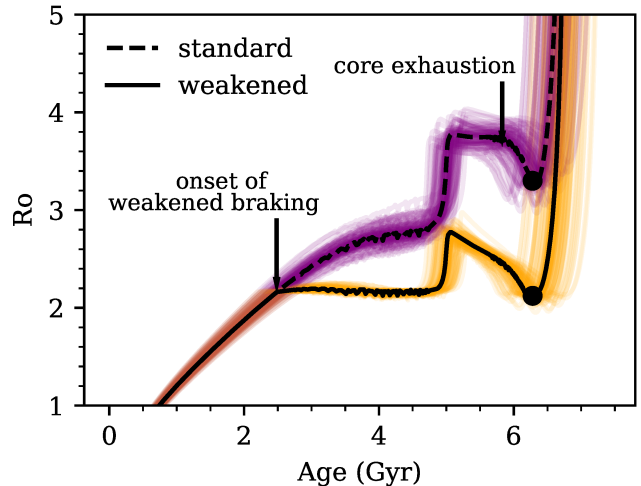
Figure 8. Predictions from a standard spin-down model (purple/dashed) and weakened braking model (orange/solid) for the evolution of the Rossby number in 94 Aqr Aa. For each model, the best-fit combination of mass and composition is shown as a dark line and the best fit age is marked with a solid point. In addition, 250 randomly drawn posterior samples of mass and composition are shown, truncated at the end of the subgiant branch.

previously been interpreted as Maunder minimum candidates (Judge et al. 2004), but at least some of them may be the end-states of large-scale stellar dynamos.

If the critical Rossby number represents a threshold above which large-scale dynamos no longer operate (Tripathi et al. 2018), then models with weakened magnetic braking may help to explain the existence of a cycle in 94 Aqr Aa. The mass of this G8 subgiant suggests that it evolved from an F-type star on the main-sequence. As such, it may have had a relatively short activity cycle until it reached the critical Rossby number after about 2.5 Gyr (see Figure 8) at a rotation period near 15 days (e.g., see Metcalfe et al. 2019, their Fig. 1). The cycle would have then grown longer and weaker for about 2 Gyr at nearly constant Rossby number. When hydrogen core-burning ceased, the core would have contracted and the star would become hotter with a thinner convection zone, pushing it above Ro_{crit} and making it a "flat activity" star. However, the star would subsequently expand and cool when hydrogen shell-burning began, slowing its rotation through conservation of angular momentum and deepening the outer convection zone. For a small range of masses above the solar value, these evolutionary effects (solid line in Figure 8) can push the Rossby number back below Ro_{crit} so the star can reinvigorate large-scale dynamo action and briefly sustain an activity cycle before ascending the red giant branch.

This scenario for a "born-again" dynamo is simply not possible with standard models (dashed line in Figure 8).

A similar mechanism may help explain the existence of magnetic cycles in subgiants that evolved from more massive F-type stars, which had never previously sustained a large-scale dynamo. For example, Egeland (2018) used Mount Wilson and Lowell observations to identify an activity cycle in the subgiant component of the HD 81809 system. The mass of this star $(1.58 \pm 0.26\ M_\odot)$ would place it above the Kraft break on the main-sequence, without a substantial outer convection zone to help build a large-scale magnetic field. Consequently, it would not have experienced significant magnetic braking during its main-sequence lifetime, and it would only have slowed to its current rotation period $(40.2 \pm 2.3$ days) through expansion on the subgiant branch. The deeper convection zone during this evolutionary phase could finally support large-scale dynamo action for the first time in its life, explaining the observed activity cycle.

The results presented above demonstrate the power of combining magnetic variability data from Mount Wilson and other programs with new asteroseismic observations from TESS. With accurate determinations of the basic stellar properties such as radius, mass, and age, we can finally reveal the evolutionary threads that connect stars with known rotation rates and magnetic activity cycles. Over the coming years, this approach promises to yield additional insights about magnetic stellar evolution, particularly beyond the middle of main-sequence lifetimes.

REFERENCES

Adelberger, E. G., Austin, S. M., Bahcall, J. N., et al. 1998, Reviews of Modern Physics, 70, 1265, doi: 10.1103/RevModPhys.70.1265

Antia, H. M., & Basu, S. 1994, A&AS, 107, 421

Baliunas, S., Sokoloff, D., & Soon, W. 1996, ApJL, 457, L99, doi: 10.1086/309891

Baliunas, S. L., Hartmann, L., Noyes, R. W., et al. 1983, ApJ, 275, 752, doi: 10.1086/161572

Baliunas, S. L., Donahue, R. A., Soon, W. H., et al. 1995, ApJ, 438, 269, doi: 10.1086/175072

Ball, W. H., & Gizon, L. 2014, A&A, 568, A123

Barnes, S. A. 2010, ApJ, 722, 222, doi: 10.1088/0004-637X/722/1/222

Benomar, O., Takata, M., Shibahashi, H., Ceillier, T., & García, R. A. 2015, MNRAS, 452, 2654, doi: 10.1093/mnras/stv1493

Böhm-Vitense, E. 2007, ApJ, 657, 486, doi: 10.1086/510482

Bonaca, A., Tanner, J. D., Basu, S., et al. 2012, ApJL, 755, L12, doi: 10.1088/2041-8205/755/1/L12

Brandenburg, A., Mathur, S., & Metcalfe, T. S. 2017, ApJ, 845, 79, doi: 10.3847/1538-4357/aa7cfa

Buzasi, D., Lezcano, A., & Preston, H. L. 2016, Journal of Space Weather and Space Climate, 6, A38, doi: 10.1051/swsc/2016033

Buzasi, D. L., Carboneau, L., Hessler, C., Lezcano, A., & Preston, H. 2015, in IAU General Assembly, Vol. 29, 2256843

Casagrande, L., Portinari, L., Glass, I. S., et al. 2014, MNRAS, 439, 2060, doi: 10.1093/mnras/stu089

Christensen-Dalsgaard, J. 2008, Ap&SS, 316, 13, doi: 10.1007/s10509-007-9675-5

Claytor, Z. R., van Saders, J. L., Santos, Â. R. G., et al. 2020, ApJ, 888, 43, doi: 10.3847/1538-4357/ab5c24

Creevey, O. L., Metcalfe, T. S., Schultheis, M., et al. 2017, A&A, 601, A67, doi: 10.1051/0004-6361/201629496

Deheuvels, S., Ballot, J., Eggenberger, P., et al. 2020, arXiv e-prints, arXiv:2007.02585. https://arxiv.org/abs/2007.02585

Deheuvels, S., & Michel, E. 2011, A&A, 535, A91, doi: 10.1051/0004-6361/201117232

Deheuvels, S., Doğan, G., Goupil, M. J., et al. 2014, A&A, 564, A27, doi: 10.1051/0004-6361/201322779

Demarque, P., Guenther, D. B., Li, L. H., Mazumdar, A., & Straka, C. W. 2008, Ap&SS, 316, 31, doi: 10.1007/s10509-007-9698-y

Denissenkov, P. A., Pinsonneault, M., Terndrup, D. M., & Newsham, G. 2010, ApJ, 716, 1269, doi: 10.1088/0004-637X/716/2/1269

Docobo, J. A., Tamazian, V. S., Campo, P. P., & Piccotti, L. 2018, AJ, 156, 85, doi: 10.3847/1538-3881/aad179

Donahue, R. A., Saar, S. H., & Baliunas, S. L. 1996, ApJ, 466, 384, doi: 10.1086/177517

Egeland, R. 2017, PhD thesis, Montana State University, Bozeman, Montana, USA

—. 2018, ApJ, 866, 80, doi: 10.3847/1538-4357/aadf86

Egeland, R., Soon, W., Baliunas, S., et al. 2017, ApJ, 835, doi: 10.3847/1538-4357/835/1/25

Fabricius, C., Høg, E., Makarov, V. V., et al. 2002, A&A, 384, 180, doi: 10.1051/0004-6361:20011822

Ferguson, J. W., Alexander, D. R., Allard, F., et al. 2005, ApJ, 623, 585, doi: 10.1086/428642

Foreman-Mackey, D., Hogg, D. W., Lang, D., & Goodman, J. 2013, PASP, 125, 306, doi: 10.1086/670067

Formicola, A., Imbriani, G., Costantini, H., et al. 2004, Physics Letters B, 591, 61, doi: 10.1016/j.physletb.2004.03.092

Fuhrmann, K. 2008, MNRAS, 384, 173, doi: 10.1111/j.1365-2966.2007.12671.x

Gaia Collaboration, Brown, A. G. A., Vallenari, A., et al. 2018, A&A, 616, A1, doi: 10.1051/0004-6361/201833051

García, R. A., Ceillier, T., Salabert, D., et al. 2014, A&A, 572, A34, doi: 10.1051/0004-6361/201423888

Gray, R. O., Corbally, C. J., Garrison, R. F., et al. 2006, AJ, 132, 161, doi: 10.1086/504637

Grevesse, N., & Sauval, A. J. 1998, SSRv, 85, 161, doi: 10.1023/A:1005161325181

Hall, J. C., Lockwood, G. W., & Skiff, B. A. 2007, AJ, 133, 862, doi: 10.1086/510356

Harvey, J. W., Hill, F., Kennedy, J. R., Leibacher, J. W., & Livingston, W. C. 1988, Advances in Space Research, 8, 117, doi: 10.1016/0273-1177(88)90304-3

Iglesias, C. A., & Rogers, F. J. 1996, ApJ, 464, 943, doi: 10.1086/177381

Jenkins, J. M., Twicken, J. D., McCauliff, S., et al. 2016, in Proc. SPIE, Vol. 9913, Software and Cyberinfrastructure for Astronomy IV, 99133E

Judge, P. G., Saar, S. H., Carlsson, M., & Ayres, T. R. 2004, ApJ, 609, 392, doi: 10.1086/421044

Katoh, N., Itoh, Y., Toyota, E., & Sato, B. 2013, AJ, 145, 41, doi: 10.1088/0004-6256/145/2/41

Kraft, R. P. 1967, ApJ, 150, 551, doi: 10.1086/149359

Kurucz, R. L. 1992, in IAU Symposium, Vol. 149, The Stellar Populations of Galaxies, ed. B. Barbuy & A. Renzini, 225

Li, T., Bedding, T. R., Kjeldsen, H., et al. 2019, MNRAS, 483, 780, doi: 10.1093/mnras/sty3000

Linsky, J. L., & Avrett, E. H. 1970, PASP, 82, 169, doi: 10.1086/128904

Lund, M. N., Handberg, R., Davies, G. R., Chaplin, W. J., & Jones, C. D. 2015, ApJ, 806, 30, doi: 10.1088/0004-637X/806/1/30

Lund, M. N., Handberg, R., Kjeldsen, H., Chaplin, W. J., & Christensen-Dalsgaard, J. 2017, in European Physical Journal Web of Conferences, Vol. 160, European Physical Journal Web of Conferences, 01005

MacGregor, K. B., & Brenner, M. 1991, ApJ, 376, 204, doi: 10.1086/170269

Magic, Z., Weiss, A., & Asplund, M. 2015, A&A, 573, A89,
    doi: 10.1051/0004-6361/201423760

Marcadon, F., Appourchaux, T., & Marques, J. P. 2018,
    A&A, 617, A2, doi: 10.1051/0004-6361/201731628

Mason, B. D., Wycoff, G. L., Hartkopf, W. I., Douglass,
    G. G., & Worley, C. E. 2001, AJ, 122, 3466,
    doi: 10.1086/323920

Mathur, S., García, R. A., Régulo, C., et al. 2010, A&A,
    511, A46, doi: 10.1051/0004-6361/200913266

Mermilliod, J. C. 2006, VizieR Online Data Catalog, II/168

Metcalfe, T. S., Kochukhov, O., Ilyin, I. V., et al. 2019,
    ApJL, 887, L38, doi: 10.3847/2041-8213/ab5e48

Metcalfe, T. S., & van Saders, J. 2017, SoPh, 292, 126,
    doi: 10.1007/s11207-017-1157-5

Montgomery, M. H., & O'Donoghue, D. 1999, Delta Scuti
    Star Newsletter, 13, 28

Mosser, B., Vrard, M., Belkacem, K., Deheuvels, S., &
    Goupil, M. J. 2015, A&A, 584, A50,
    doi: 10.1051/0004-6361/201527075

Mosser, B., Benomar, O., Belkacem, K., et al. 2014, A&A,
    572, L5, doi: 10.1051/0004-6361/201425039

Olspert, N., Lehtinen, J. J., Käpylä, M. J., Pelt, J., &
    Grigorievskiy, A. 2018, A&A, 619, A6,
    doi: 10.1051/0004-6361/201732525

Paunzen, E. 2015, A&A, 580, A23,
    doi: 10.1051/0004-6361/201526413

Paxton, B., Bildsten, L., Dotter, A., et al. 2011, ApJS, 192,
    3, doi: 10.1088/0067-0049/192/1/3

Ricker, G. R., Winn, J. N., Vanderspek, R., et al. 2014, in
    Society of Photo-Optical Instrumentation Engineers
    (SPIE) Conference Series, Vol. 9143, Proceedings of the
    SPIE, Volume 9143, id. 914320 15 pp. (2014)., 914320

Rogers, F. J., & Nayfonov, A. 2002, ApJ, 576, 1064,
    doi: 10.1086/341894

Saio, H., Kurtz, D. W., Takata, M., et al. 2015, MNRAS,
    447, 3264, doi: 10.1093/mnras/stu2696

Sarma, M. B. K. 1962, ApJ, 135, 301, doi: 10.1086/147268

Schofield, M., Chaplin, W. J., Huber, D., et al. 2019, ApJS,
    241, 12, doi: 10.3847/1538-4365/ab04f5

Serenelli, A., Johnson, J., Huber, D., et al. 2017, ApJS,
    233, 23, doi: 10.3847/1538-4365/aa97df

Shibahashi, H. 1979, PASJ, 31, 87

Somers, G., & Pinsonneault, M. H. 2016, ApJ, 829, 32,
    doi: 10.3847/0004-637X/829/1/32

Soon, W. H., Baliunas, S. L., & Zhang, Q. 1994, SoPh, 154,
    385, doi: 10.1007/BF00681107

Stassun, K. G., Collins, K. A., & Gaudi, B. S. 2017, AJ,
    153, 136, doi: 10.3847/1538-3881/aa5df3

Stassun, K. G., Corsaro, E., Pepper, J. A., & Gaudi, B. S.
    2018, AJ, 155, 22, doi: 10.3847/1538-3881/aa998a

Stassun, K. G., & Torres, G. 2016, ApJL, 831, L6,
    doi: 10.3847/2041-8205/831/1/L6

—. 2018, ApJ, 862, 61, doi: 10.3847/1538-4357/aacafc

Steigman, G. 2010, JCAP, 4, 029.
    https://arxiv.org/abs/1002.3604

Tayar, J., Somers, G., Pinsonneault, M. H., et al. 2017,
    ApJ, 840, 17, doi: 10.3847/1538-4357/aa6a1e

Thompson, M. J., Toomre, J., Anderson, E. R., et al. 1996,
    Science, 272, 1300, doi: 10.1126/science.272.5266.1300

Thoul, A. A., Bahcall, J. N., & Loeb, A. 1994, ApJ, 421,
    828, doi: 10.1086/173695

Tokovinin, A., Mason, B. D., Hartkopf, W. I., Mendez,
    R. A., & Horch, E. P. 2015, AJ, 150, 50,
    doi: 10.1088/0004-6256/150/2/50

Tripathi, B., Nandy, D., & Banerjee, S. 2018, arXiv
    e-prints, arXiv:1812.05533.
    https://arxiv.org/abs/1812.05533

van Saders, J. L., Ceillier, T., Metcalfe, T. S., et al. 2016,
    Nature, 529, 181, doi: 10.1038/nature16168

van Saders, J. L., & Pinsonneault, M. H. 2013, ApJ, 776,
    67, doi: 10.1088/0004-637X/776/2/67

van Saders, J. L., Pinsonneault, M. H., & Barbieri, M.
    2019, ApJ, 872, 128, doi: 10.3847/1538-4357/aafafe

VandenBerg, D. A., & Clem, J. L. 2003, AJ, 126, 778,
    doi: 10.1086/376840

Vaughan, A. H., Preston, G. W., & Wilson, O. C. 1978,
    PASP, 90, 267, doi: 10.1086/130324

Viani, L. S., Basu, S., Ong J., M. J., Bonaca, A., & Chaplin,
    W. J. 2018, ApJ, 858, 28, doi: 10.3847/1538-4357/aab7eb

White, O. R., & Livingston, W. C. 1981, ApJ, 249, 798,
    doi: 10.1086/159338

White, T. R., Huber, D., Mann, A. W., et al. 2018,
    MNRAS, 477, 4403, doi: 10.1093/mnras/sty898

Wilson, O. C. 1978, ApJ, 226, 379, doi: 10.1086/156618

Zinn, J. C. 2019, in American Astronomical Society
    Meeting Abstracts, Vol. 233, American Astronomical
    Society Meeting Abstracts #233, 341.07